Accurate Predictions of Hovering Rotor Flows Using CFD

A. Jimenez Garcia[a], S. Colonia[b], G.N. Barakos[c]
CFD Laboratory, School of Engineering, University of Glasgow, G12 8QQ Glasgow, UK

With work on the S-76 rotor providing encouraging results regarding the prediction of integral loads with CFD in hover, the XV-15 rotor is now analysed. Fully turbulent and transitional results are obtained showing the capability of modern CFD methods. The transition onset and distribution of skin friction are well predicted and were found to have a mild effect on the overall figure of merit. This work also shows the potential of transport-based models for transition prediction in complex 3D flows. Finally, hover simulations for the PSP blade are also shown in terms of surface pressure coefficient and wake visualisation.

Nomenclature

$\boldsymbol{R}$	=	flow equation residual vector
$\boldsymbol{W}$	=	flow solution vector
a_∞	=	freestream speed of sound, *m/s*
c	=	rotor blade chord
c_{ref}	=	reference blade chord
C_P	=	blade section pressure coefficient, $C_P = \dfrac{P - P_\infty}{1/2\rho_\infty(\Omega r)^2}$
C_P^*	=	critical pressure coefficient
C_Q	=	rotor torque coefficient, $C_Q = \dfrac{Q}{\rho_\infty(\Omega R)^2\pi R^3}$
C_q	=	blade section torque coefficient, $C_q = \dfrac{\mathrm{d}C_Q}{\mathrm{d}r}$
C_Q/σ	=	blade torque coefficient, torque coefficient divided by rotor solidity
C_t	=	blade section thrust coefficient, $C_t = \dfrac{\mathrm{d}C_T}{\mathrm{d}r}$
C_T	=	rotor thrust coefficient, $C_T = \dfrac{T}{\rho_\infty(\Omega R)^2\pi R^2}$
C_T/σ	=	blade loading coefficient, thrust coefficient divided by rotor solidity

[a] PhD Student, CFD Laboratory, School of Engineering, Email: a.jimenez-garcia.1@research.gla.ac.uk
[b] Research Associate, CFD Laboratory, School of Engineering, Email: Simone.Colonia@glasgow.ac.uk
[c] Professor, MAIAA, MRAeS, CFD Laboratory, School of Engineering, Email: George.Barakos@glasgow.ac.uk

C_{DO} = overall profile drag coefficient

k = turbulent kinetic energy

k_i = induced power factor

M_{tip} = blade-tip Mach number, $M_{\text{tip}} = \dfrac{V_{\text{tip}}}{a_\infty}$

N_{b} = number of blades

P = pressure

P_∞ = freestream pressure

Q = rotor torque

R = rotor radius

r = radial coordinate along the blade span

Re = Reynolds number, Re $= V_{\text{tip}} c_{\text{ref}} / \nu_\infty$

Re_θ = momentum thickness Reynolds number

T = rotor thrust

V_{tip} = blade-tip speed, $V_{\text{tip}} = \Omega R$

FoM = figure of merit, FoM = $\dfrac{C_T^{3/2}}{\sqrt{2} C_Q}$

γ = intermittency factor

ν_∞ = freestream kinematic viscosity

Ω = rotor rotational speed

ρ_∞ = freestream density

σ = rotor solidity, $\sigma = \dfrac{N_b c_{\text{ref}}}{\pi R}$

Θ = local blade twist angle

θ_{75} = blade pitch angle at r/R = 0.75

ALE = arbitrary Lagrangian Eulerian

ATB = advanced technology blade

BILU = block incomplete lower upper

CFD = computational fluid dynamics

CFL = Courant Friedrichs Lewy

DDES = delayed detached eddy simulation

DES = detached eddy simulation

HMB = helicopter multi-block

LES = large eddy simulation

MUSCL = monotone upstream centred schemes for conservation laws

OARF = outdoor aerodynamic research facility

PSP = pressure sensitive paint

RANS = Reynolds averaged Navier-Stokes

SA = Spalart Allmaras

SST = shear stress transport

VTOL = vertical take-off landing

∞ = freestream value

tip = blade-tip value

* = sonic condition

I. Introduction

Tiltrotor is a flying vehicle that combines VTOL (vertical take-off/landing) capability with high speed cruise. Tiltrotors were successfully demonstrated in United States with the Bell XV-3, which first flew in 1955[1]. In the late 1960s and early 1970s, the XV-15 tiltrotor was developed, and was followed by modern tiltrotors like the Bell-Boeing V-22 Osprey[2, 3] and the AW609[4, 5] which is currently undergoing certification.

Very little wind tunnel data is available for model and full-scale tiltrotors. At the early stage of the XV-15 program, the NASA 40-by-80-Foot Wind Tunnel was used to measure integrated rotor loads in helicopter[6], aeroplane and transition-corridor modes[7]. However, force and moment measurements did not exclude the contribution from the airframe. The NASA-Ames Outdoor Aeronautical Research Facility (OARF) was also extensively used by Felker *et al.*[8] with the XV-15 rotor and Bartie *et al.*[9] with the XV-15 Advanced Technology Blade (ATB). The hover and forward flight tests began in the late 90s with the work of Light[10] in the 80-ft by 120-ft wind tunnel at NASA Ames, but only few conditions were tested. To fill this gap, Betzina[11] in 2002 undertook an extensive campaign of experiments on the full-scale XV-15 rotor, where the experiments were corrected for hub and tares effects.

For all set of experiments cited, neither surface pressure nor skin friction coefficients were measured. In this regard, Wadcook *et al.*[12] measured skin friction coefficients on a hovering full-scale XV-15 tiltrotor in the 80-ft by 120-ft wind tunnel at NASA Ames. At low thrust, an extension region of laminar flow was encountered over a significant fraction of the blade chord, while at high disc loading conditions, the laminar to turbulent transition region on the upper blade surface moved towards the blade leading edge, with fully turbulent boundary layer encountered at outboard section. This set of experiments could be employed to validate and improve transitional models for tiltrotors.

Concerning numerical simulations of tiltrotor blades, Kaul *et al.*[13, 14] studied the effect of inflow boundary conditions and turbulent models on the hovering XV-15 rotor blade, using the OVERFLOW2 CFD solver. Results with the Spalart-Allmaras model [15] with the Detached Eddy Simulation formulation, revealed a lack of agreement with the experiments of Wadcook *et al.*[12] in the laminar-turbulent transitional region. Likewise, Yoon *et al.*[16] investigated the effect of the employed turbulence model on the hovering performance and skin friction coefficients of the XV-15 rotor blade at a collective of 10°. It was found that the $k-\omega$ SST-DDES turbulence model predicted the figure of merit closer to experiment that the SA-DDES one-equation model. However, minimal differences between these fully-turbulent models were observed in the predictions of skin friction coefficient, which did not reproduce well the flowfield encountered in the experiment[12]. Sheng *et al.*[17] used the U^{2}NCLE and Helios CFD solvers to assess the effect of transition models in predicting the hover figure of merit on the XV-15 blade. Despite the use of a grid size of 294 million cells for the whole rotor, results at 10° collective showed an over-predicted FoM with a discrepancy of 3.17%. It was shown that the transitional flow modelling did not have a significant impact on the predicted FoM mainly due to the small laminar-turbulent transition region encountered on the XV-15 blades. A detailed performance analysis of the hover and propeller modes of the XV-15 blades were performed by Gates[18]

using the HMB CFD solver. Good agreement with published experimental data was reported, even though a medium grid size (9.6 million cells per blade) was employed for computations. Furthermore, the effect of the hub spinner on the propeller performance at moderate advance ratios was highlighted.

Further studies have also been published for the V-22 tiltrotor using numerical simulations. The drag polar of the V-22 aircraft has been measured in the 20x20ft Boeing wind tunnel[19] and the results were compared against CFD predictions of the FUN3D and OVERFLOW CFD codes. Neither CFD nor experiments considered the effect of the rotors. The experiments considered a model of the V-22 of 0.15 scale and provided integrated lift, drag and moment data. In general, the authors stated that good agreement between the CFD and experiments was obtained even if further studies were recommended to ensure that mesh independent results can be obtained.

In this work, we present an aerodynamic study of the XV-15 tiltrotor blades with high-fidelity computational fluid dynamics. The aim is to assess the level of accuracy of the present CFD method in predicting the figure of merit for a hover case. This is addressed by comparing with experimental data available in the literature[8, 10, 11]. To reduce the computational cost, we solved the hover flow by casting the equations as a steady-state problem in a noninertial reference frame. Results are presented for a range of design points, which includes medium and high thrust hover conditions. The second objective is to investigate the impact of a fully-turbulent k-ω SST and transitional k-ω SST-γ models on the predicted figure of merit at collective angles of 3° and 10°. Moreover, the ability of those models in predicting the experimental skin friction distribution[12] on the blade surface is also discussed.

Due to the lack of surface pressure data for the XV-15 blade, the Pressure Sensitive Paint (PSP) blade is also considered. This blade has so far been used for experiments that compared PSP data with measurements using Kulite pressure transducers [20], and is to be re-used for further tests in hover as part of a future campaign that will be conducted in the USA.

II. CFD Method

A. HMB Solver

The Helicopter Multi-Block (HMB)[21–23] code is used as the CFD solver for the present work. It solves the Unsteady Reynolds Averaged Navier-Stokes (URANS) equations in integral form using the Arbitrary Lagrangian Eulerian (ALE) formulation for time-dependent domains, which may include moving boundaries. The Navier-Stokes equations are discretised using a cell-centred finite volume approach on a multi-block grid. The spatial discretisation of these equations leads to a set of ordinary differential equations in time,

$$\frac{d}{dt}(\boldsymbol{W}_{i,j,k}\, V_{i,j,k}) = -\boldsymbol{R}_{i,j,k}(\boldsymbol{W}) \tag{1}$$

where i, j, k represent the cell index, $\boldsymbol{W}$ and $\boldsymbol{R}$ are the vector of conservative flow variables and flux residual respectively, and $V_{i,j,k}$ is the volume of the cell i, j, k. To evaluate the convective fluxes, Osher[24] and Roe[25] approximate Riemann solvers are used in HMB, while the viscous terms are discretised using a

second order central differencing spatial discretisation. The Monotone Upstream-centred Schemes for Conservation Laws, which is referred to in the literature as the MUSCL approach and developed by Leer[26], is used to provide third order accuracy in space. The HMB solver uses the alternative form of the Albada limiter[27] being activated in regions where a large gradients are encountered mainly due to shock waves, avoiding the non-physical spurious oscillations. An implicit dual-time stepping method is employed to performed the temporal integration, where the solution is marching in pseudo-time iterations to achieve fast convergence, which is solved using a first-order backward difference. The linearised system of equations is solved using the Generalised Conjugate Gradient method with a Block Incomplete Lower-Upper (BILU) factorisation as a pre-conditioner[28]. To allow an easy sharing of the calculation load for parallel job, a multi-block structured meshes are used.

B. Turbulence Models

Various turbulence models are available in HMB solver, including several one-equation, two-equation, three-equation, and four-equation turbulence models. Furthermore, Large-Eddy Simulation (LES), Detached-Eddy Simulation (DES) and Delay-Detached-Eddy Simulation (DDES) are also available. For this study, two and three equations models were employed using the fully-turbulent k-ω SST and the transitional model k-ω SST-γ both from Menter[29, 30]. It is well known that the fully-turbulent k-ω SST model predicts the transition onset further upstream than nature, being needed the use of transitional models. In this regard, Menter *et al.*[31] developed a model for the prediction of laminar-turbulent transition flows, involving two transport equations for the intermittency factor γ and the momentum thickness Reynolds number Re_θ. The intermittency factor γ is used to trigger and control the transition onset location, and value varies between 0 (laminar flow) to 1 (fully-turbulent flow). In 2015, a new one-equation local correlation-based transition model γ was proposed by Menter *et al.*[30], where the Re_θ equation was avoided. The form of the transport equation for the intermittency factor γ reads as:

$$\frac{\partial(\rho\gamma)}{\partial t} + \frac{\partial(\rho U_j\gamma)}{\partial x_j} = P_\gamma - E_\gamma + \frac{\partial}{\partial x_j}\left[\left(\mu + \frac{\mu_t}{\sigma_\gamma}\right)\frac{\partial\gamma}{\partial x_j}\right] \tag{2}$$

where P_γ and E_γ represent the production and destruction sources, respectively. A more detailed description of the γ equation can be found in Menter *et al.*[30].

III. Rotor Geometry and Mesh Generation

A. XV-15 Rotor Geometry

The three-bladed XV-15 rotor geometry was generated based on the full-scale wind tunnel model performed by Betzina in the NASA Ames 80- by 120-foot wind tunnel facility[11]. NACA 6-series, five-digit aerofoil sections comprise the rotor blade (see Table 1).

The main geometric characteristics of the XV-15 rotor blades[11] are summarised in Table 2. Unlike convectional helicopter blades, tiltrotor blades are characterised by a high linear twist angle ($\Theta = -40.25°$) and rotor solidity ($\sigma = 0.089$) along with a small rotor radius ($R = 150$ inches).

$\mathbf{r/R}$	**Aerofoil**
0.09	NACA 64-935
0.17	NACA 64-528
0.51	NACA 64-118
0.80	NACA 64-(1.5)12
1.00	NACA 64-208

Table 1: Radial location of the XV-15 rotor blade aerofoils[8].

Parameter	**Value**
Number of blades (N_b)	3
Rotor radius (R)	150 inches
Rotor blade chord (c)	14 inches
Aspect ratio (R/c)	10.71
Rotor solidity (σ)	0.089
Linear twist angle (Θ)	-40.25°

Table 2: Geometric properties of the full-scale XV-15 rotor[11].

A detailed sketch of the XV-15 blade planform and the blade radial twist, and chord distributions are shown in Figure 1. The rotor blade chord is held constant, and extends at almost 80% of the rotor blade. The blade root, however, was not modelled due to the lack of information on the cuff geometry in the literature.

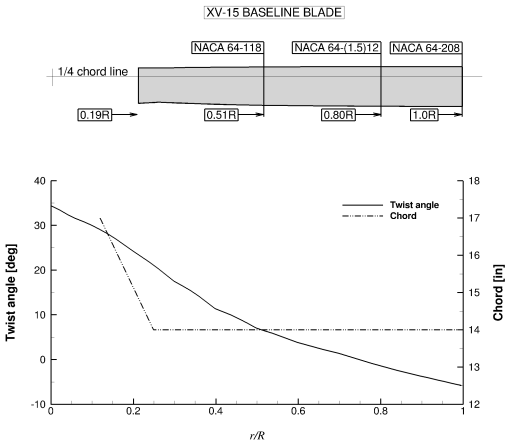

Fig. 1: Planform of the XV-15 rotor blade (above) and twist and chord distributions[32] (below).

B. XV-15 Rotor Mesh

A mesh generated using the Chimera technique was used for the aerodynamic study of the XV-15 rotor, and it was composed by a Cartesian off-body mesh used as background and a body-fitted mesh for the blade. The use of an overset grid method allowed for the blade pitch angle to be changed by rotating the body-fitted

mesh. The flow around the hovering XV-15 rotor was solved as a steady-state problem, and only a third of the computational domain was meshed, assuming periodic conditions for the flowfield in the azimuthal direction. A view of the computational domain along with the employed boundary conditions is given in Figure 2 (a). Farfield boundaries were extended to $2R$ (above rotor) and $4R$ (below rotor and in the radial direction) from the rotor plane, which is only adequate with the boundary conditions employed. Furthermore, an ideal rotor hub was modelled and approximated as a cylinder, extending from inflow to outflow with a radius of $0.05R$.

A C-topology was selected for the leading edge of the blade, while an H-topology was employed at the trailing edge. This configuration permits an optimal resolution of the boundary layer due to the orthogonality of the cells around the surface blade (see Figure 2 (b)). The height of the first mesh layer above the blade surface was set to $1.0 \cdot 10^{-5} c_{\text{ref}}$, which leads to y^+ less than 1.0 all over the blade. Considering the chordwise and spanwise directions of the blade, 264 and 132 mesh points were used, whilst the blunt trailing-edge was modelled with 42 mesh points.

To guarantee a mesh independent solution, two computational domains were built. Table 5 lists the grids used and shows the breakdown of cells per blade. Coarse and medium meshes have 6.2 and 9.6 million cells per blade (equivalent to 18.6 and 28.8 million cells for three blades), with the same grid resolution for the body-fitted mesh (3.6 million cells). The background mesh, however, was refined at the wake and near-body regions, increasing the grid size from 2.6 to 6 million cells.

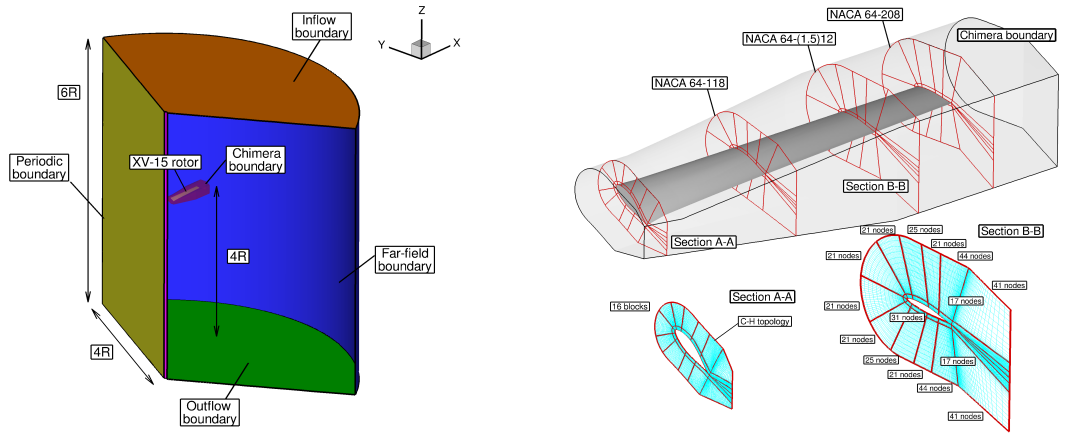

(a) Computational domain.

(b) XV-15 rotor mesh.

Fig. 2: Computational domain and boundary conditions employed (left) and detailed view of the XV-15 rotor mesh (right).

C. PSP Rotor Geometry

The four-bladed PSP rotor has an aspect ratio (R/c) of 12.2 and a nominal twist of -14 degrees. The main characteristics of the rotor blades are summarised in Table 4. The blade planform has been generated using three radial stations. First, the RC(4)-12 aerofoil was used up to 65% R. Then, the RC(4)-10 aerofoil from 70% R to 80% R. Finally, the RC(6)-08 aerofoil was used from 85% R to the tip. The aerodynamic characteristics of these aerofoils can be found in [33, 34].

	Coarse Mesh	Medium Mesh
Background mesh size (cells)	2.6 million	6.0 million
Blade mesh size (cells)	3.6 million	3.6 million
Overall mesh size (cells)	6.2 million	9.6 million
Height of the first mesh layer at blade surface	$1.0 \cdot 10^{-5} c_{\text{ref}}$	$1.0 \cdot 10^{-5} c_{\text{ref}}$

Table 3: Meshing parameters for the XV-15 rotor mesh.

Parameter	Value
Number of blades (N_{b})	4
Rotor radius (R)	66.50 inches
Rotor blade chord (c)	5.45 inches
Aspect ratio (R/c)	12.2
Rotor solidity (σ)	0.104
Linear twist angle (Θ)	-14°

Table 4: Geometric properties of the PSP rotor[20].

D. PSP Rotor Mesh

Like for the XV-15 rotor, a mesh generated using the Chimera technique was used for the aerodynamic study of the PSP rotor. Only a quarter of the computational domain was meshed, assuming periodic conditions for the flowfield in the azimuthal direction. A view of the computational domain along with the employed boundary conditions is given in Figure 3. The meshing parameters for the PSP mesh rotor blade along with the grids used are shown in Table 5.

	Medium Mesh
Background mesh size (cells)	7.2 million
Blade mesh size (cells)	5.2 million
Overall mesh size (cells)	12.4 million
Height of the first mesh layer at blade surface	$1.0 \cdot 10^{-5} c_{\text{ref}}$
Points along the span	215
Points around the aerofoil	252

Table 5: Meshing parameters for the PSP rotor mesh.

IV. Test Conditions and Computations

A. XV-15 Computations

The hovering flight condition was selected from the available literature on the XV-15 [8, 10, 11]. The tip Mach number was set to 0.69, and four collective angles were considered, covering low, medium, and high disc loadings. The Reynolds number, based on the reference blade chord of 14 inches and on the tip speed, was $4.95 \cdot 10^6$.

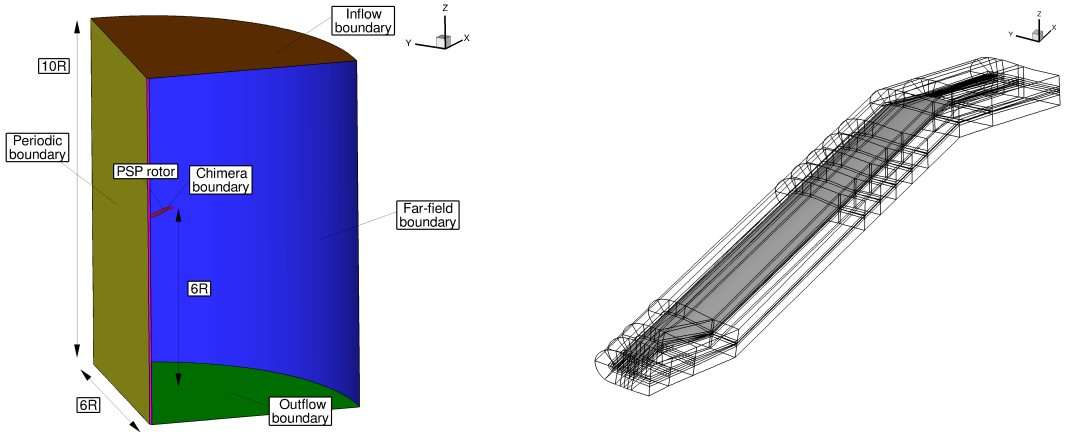

(a) Computational domain.

(b) PSP rotor mesh.

Fig. 3: Computational domain and boundary conditions employed (left) and topology of the PSP rotor mesh (right).

All flow solutions were computed by solving the RANS equations, coupled with Menter's $k-\omega$ SST turbulence model[29]. The flow equations were integrated with the implicit dual-time stepping method of HMB, using a pseudotime Courant–Friedrichs–Lewy (CFL) equal to 4. Typically, 40,000 iterations were necessary to drop the residual by 6 orders of magnitude for the flow solutions. Table 6 lists the flow conditions employed for the aerodynamic study of the XV-15 tiltrotor blade.

Blade-tip Mach number (M_{tip})	0.69
Reynolds number (Re)	$4.95 \cdot 10^6$
Blade pitch angle (θ_{75})	3,5,10,13
Grid	Coarse and Medium
Turbulence model	k-ω SST

Table 6: Flow conditions for the full-scale XV-15 tiltrotor blade.

B. PSP Computations

Regarding the PSP blade, the tip Mach number was set to 0.65, and seven collective angles were considered, covering low, medium, and high disc loadings. The Reynolds number, based on the reference blade chord of 5.45 inches and on the tip speed, was $2.16 \cdot 10^6$. Like the XV-15 blade, all flow solutions were computed by solving the RANS equations, coupled with Menter's $k-\omega$ SST turbulence model[29].

V. Results and Discussions

A. Results for the XV-15 Rotor

1. Mesh Convergence

The effect of the mesh density on the figure of merit, and torque coefficient as functions of the thrust coefficient are shown in Figure 4. Experimental data of the full-scale XV-15 rotor is also shown, carried out by Felker *et al.*[8] at the Outdoor Aerodynamic Research Facility (OARF), and Light[10] and Betzina[11] at the NASA 80x120ft wind tunel. The majority of works on performance analysis of rotor blades do not model the hub and apparatus tares, mainly due to the complexity of mesh generation. In this regard, experiments were corrected for hub and apparatus tares effects [11]. Vertical lines labeled as empty (4,574 kg) and maximum gross (6,000 kg) weight, define the hovering range of the XV-15 helicopter rotor[1], which highlights a limited hovering operational range. Momentum-based estimates of the figure of merit are also included and its expression is given in Equation 3, where an induced power factor k_i of 1.1 and overall profile drag coefficient C_D of 0.01 were used. This theory, is limited to low and medium thrust, leading to a wrong trend of the power divergence, due to flow separation[35].

$$\text{FoM} = \frac{{C_T}^{3/2}}{\sqrt{2}\left(\sigma\frac{C_D}{8} + k_i\frac{{C_T}^{3/2}}{\sqrt{2}}\right)} \tag{3}$$

Solutions with the coarse and medium grids (represented with square and triangle symbols) were established by second-order least-squares. Considering the set of experiments, an overall good agreement was found between all of them, with a maximum discrepancy of 4.11% in figure of merit. The reason for this disagreement (4 counts FoM) may be partly due to the variations in experimental data between wind tunnel facilities. CFD results present an excellent agreement with the test data of Betzina[11] for all blade collective angles. It is found that the effect of the grid size on the overall performance is negligible at low thrust, with a small influence a high thrust.

To quantify the accuracy of the present CFD method in capturing the peak figure of merit, a comparison between predicted and measured [8, 10, 11] peak FoM and its percent change % (with respect to Betzina's experiments) is reported in Table 7. It is interesting to note that both Betzina and Light's experiments have the same peak FoM, while Felker's experiments show a higher peak figure of merit (2.7 counts) if compared with Betzina's experiments. A large recirculation zone was reported in the 80x120 test section of NASA by Felker, which may be the reason of this disagreement. Predictions with the medium grid indicate good correlation with the experiments (0.91% with Betzina and Light, and 2.53% with Felker), which highlights the ability of this medium grid in accurately predicting the peak of FoM with a modest CPU time.

From a point of view of the turbulent model employed, it seems that the fully turbulent flow assumption is able to capture the trend of FoM and torque coefficient (see Figure4 (b)). Similar conclusions were drawn in previous works by Kaul *et al.*[13], Yoon *et al.*[16], and Sheng *et al.*[17], where fully turbulent flows were successfully employed.

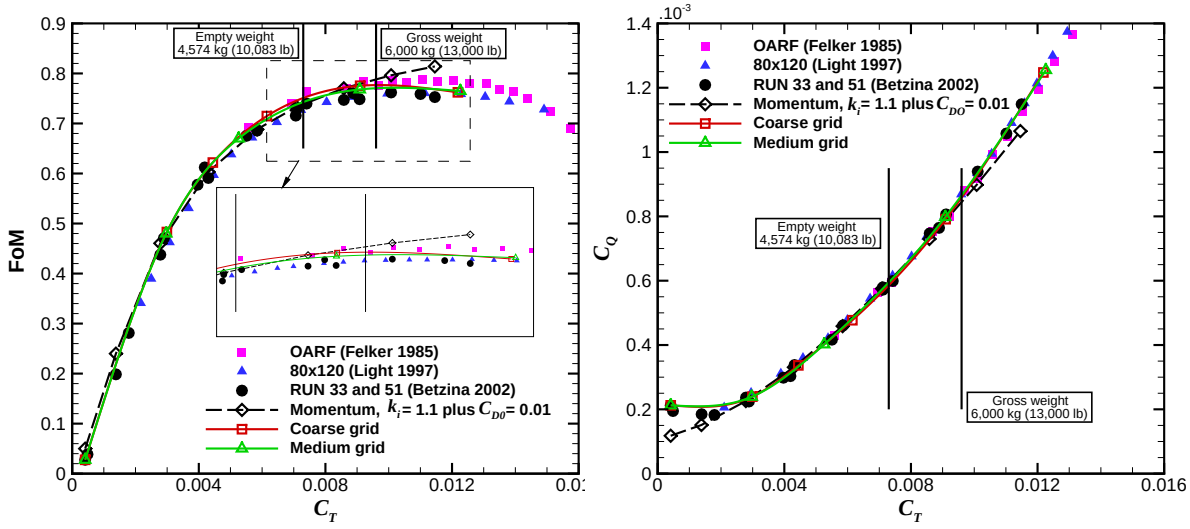

(a) FoM - C_T.

(b) C_Q - C_T.

Fig. 4: Effect of the mesh density on the figure of merit (left) and torque coefficient (right) for the full-scale XV-15 rotor. Conditions employed: $M_{\text{tip}} = 0.69$, $Re = 4.95 \cdot 10^6$, and Menter's k-ω SST turbulence model[29].

	FoM	**ΔFoM**[%]
Felker *et al.*[8]	0.788	3.54
Light[10]	0.761	-
Betzina[11]	0.761	-
Coarse mesh	0.776	1.97
Medium mesh	0.768	0.91

Table 7: Comparison of the predicted and experimental peak FoM for the full-scale XV-15 rotor. Conditions employed: $M_{\text{tip}} = 0.69$, $Re = 4.95 \cdot 10^6$, and Menter's k-ω SST turbulence model[29].

2. *Surface Pressure Predictions*

Due to the lack of experimental surface pressure measurements, a comparison between HMB and CFD data published by Kaul *et al.*[14] using the OVERFLOW2 solver at three radial stations (r/R=0.72, 0.83, and 0.94) was carried out, and it is shown in Figure 5. CFD results using HMB correspond to the coarse grid (18.6 million cells for the three blades) where the k-ω SST turbulence model[29] was employed, while Kaul's results were obtained with a grid size of 35 million cells using the Spalart-Allmaras turbulence model[36]. Despite that a variation on the predicted peak C_P seen by the different numerical simulations, a fair agreement is found for all radial stations. Regarding the radial stations $r/R = 0.72$ and $r/R = 0.83$, it is clear that the suction peak does not exceeded the critical C_P^* values, while the most outboard section ($r/R = 0.94$), reaches sonic conditions.

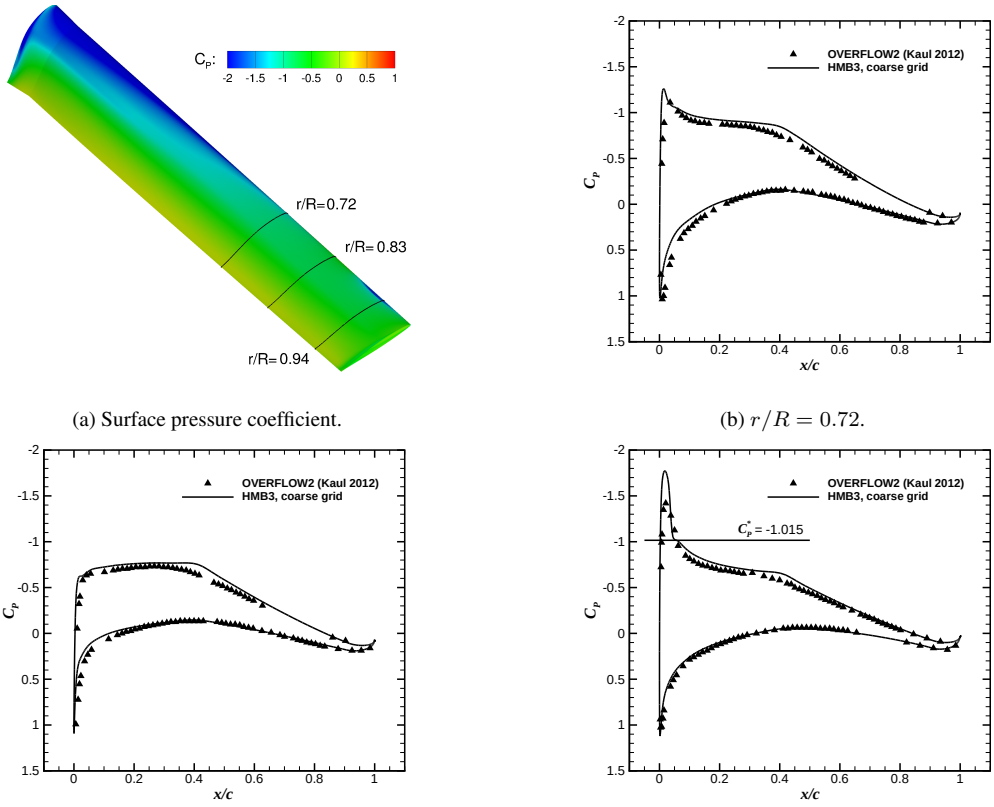

(a) Surface pressure coefficient.

(b) $r/R = 0.72$.

(c) $r/R = 0.83$.

(d) $r/R = 0.94$.

Fig. 5: Comparison of predicted surface pressure coefficients between HMB using a coarse grid and OVERFLOW2 from Kaul *et al.*[14]. Conditions employed: $M_{\text{tip}} = 0.69$, $Re = 4.95 \cdot 10^6$, and $\theta_{75} = 10°$.

3. Sectional Loads

Figure 6 shows the distribution of blade section thrust and torque coefficients along the rotor radius for collective pitch angles from $3°$ to $13°$. The influence of the tip vortex on the tip region (from $0.92R$ to $1.0R$) is visible in terms of loading and torque coefficients.

4. Effect of the Turbulence Model

In this study, the effect of the k-ω SST-γ transition model is investigated in predicting the figure of merit. The predicted skin friction coefficient is compared with measurements by Wadcock *et al.*[12]. Moreover, a comparison with the solution obtained with the fully-turbulent k-ω SST model is presented.

Figures 7 and 8 show the computed skin friction coefficient C_f compared with the available experimental data of Wadcock *et al.*[37] for collective pitch angles of $3°$ and $10°$ at the radial stations $r/R = 0.28, 0.50, 0.72, 0.83$ and 0.94. At low disc loading (Figure 7), the experiment shows a natural transition for all stations at about 50% chord. It seems that the present transition model is able to capture the onset and length of the natural transition with some discrepancies found at the inboard station $r/R = 0.28$. As

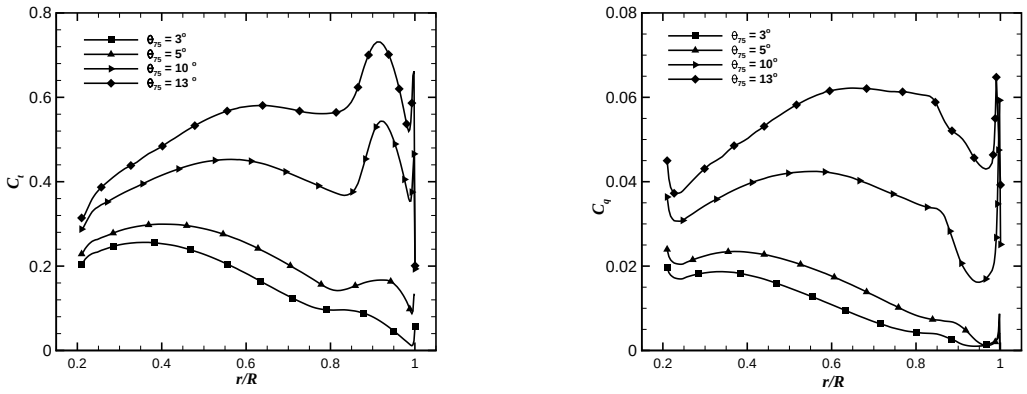

(a) (b)

Fig. 6: Blade section thrust (left) and torque (right) coefficient along the rotor radius for the XV-15 rotor blade. Conditions employed: $M_{\text{tip}} = 0.69$, $Re = 4.95 \cdot 10^6$, and Menter's k-ω SST turbulence model [29].

expected, results obtained with the fully-turbulent model indicate lack of transition. Moreover, the values of skin friction coefficient are under and over-predicted in the laminar and turbulent flow regions. Considering the C_f at collective pitch angle of 10° (Figure 8), the experimental C_f presents a similar pattern as seen for the lower collective pitch angles. However, the onset of the natural transition is moved towards the blade leading edge, with a fully-turbulent flow region observed at the outboard station $r/R = 0.94$. Results corresponding to the transition model accurately predicted the onset location and length of the transition. This phenomenon is not captured for the fully-turbulent solution. The surface skin friction coefficient of both turbulence models is shown in Figure 9, where the laminar-turbulent region can be only identified for the k-ω SST-γ model.

The impact of the turbulence model on the hovering performance of the XV-15 blade is now investigated. Table 8 reports the predicted C_T, C_Q, and FoM using the fully-turbulent $k-\omega$ SST and transitional model k-ω SST-γ at two disc loading conditions. It is shown that results are sensitive to the turbulence model employed, with a high figure of merit presented by the transitional model.

	$\mathbf{C_T}$	$\mathbf{C_Q}$	**FoM**
FT 3°	0.00293	0.000249	0.450
TM 3°	0.00297	0.000223	0.512
FT 10°	0.00906	0.000807	0.756
TM 10°	0.00909	0.000803	0.763

Table 8: Comparison of predicted C_T, C_Q, and FoM at 3° and 10° collective angles between the fully-turbulent k-ω SST and transition model k-ω SST-γ. Conditions employed: $M_{\text{tip}} = 0.69$ and $Re = 4.95 \cdot 10^6$. FT=Fully-Turbulent; TM=Transitional-Model.

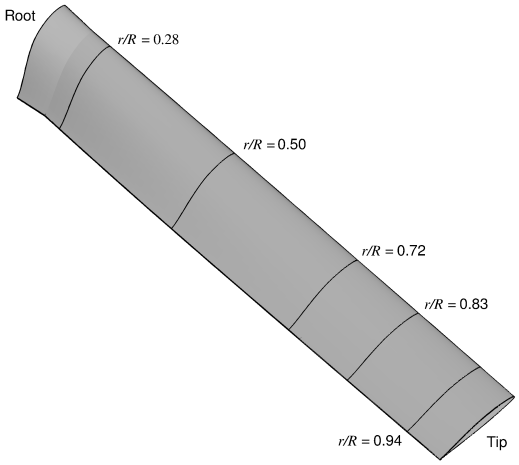

(a) Radial stations.

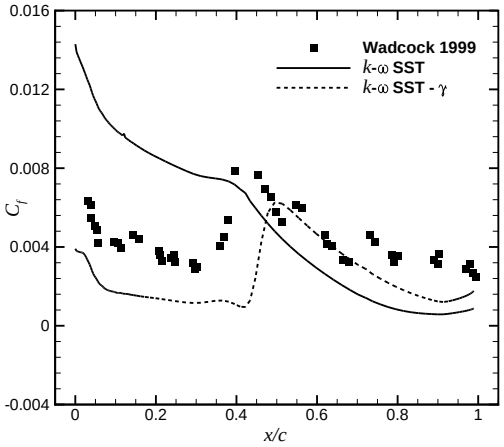

(b) $r/R = 0.28$.

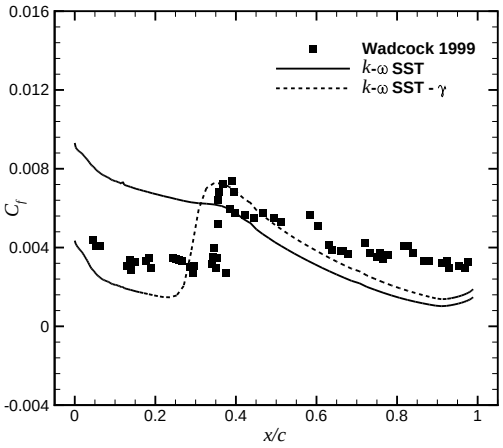

(c) $r/R = 0.50$.

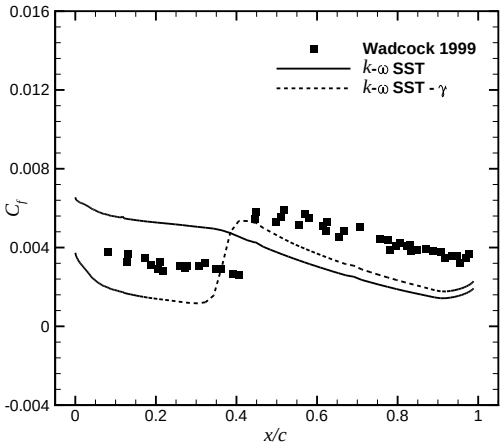

(d) $r/R = 0.72$.

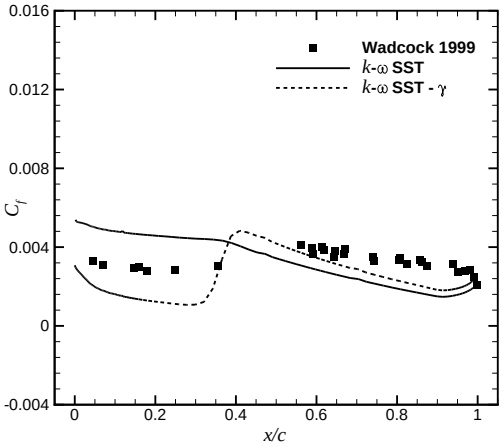

(e) $r/R = 0.83$.

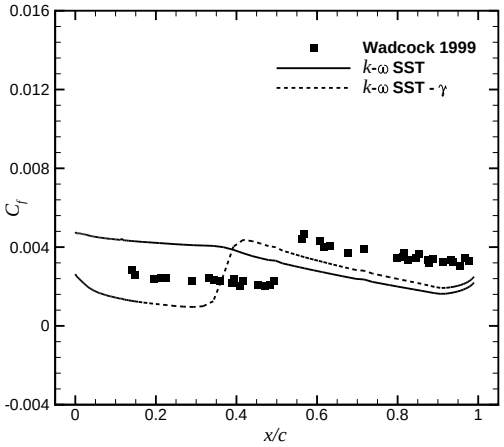

(f) $r/R = 0.94$.

Fig. 7: Comparison between the computed skin friction coefficient using a fully turbulent and transition model solutions with the experimental data of Wadcock *et al.*[37]. Conditions employed: $M_{\text{tip}} = 0.69$, $Re = 4.95 \cdot 10^6$, and $\theta_{75} = 3°$.

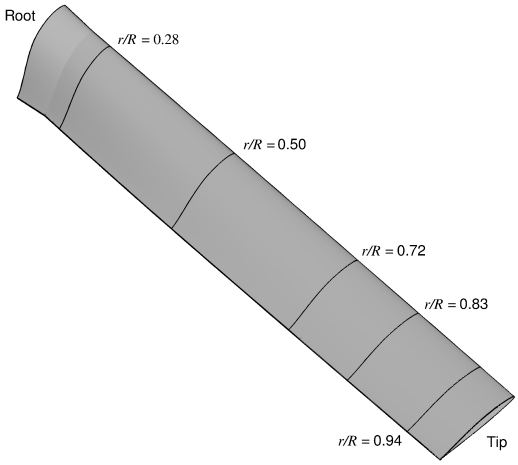

(a) Radial stations.

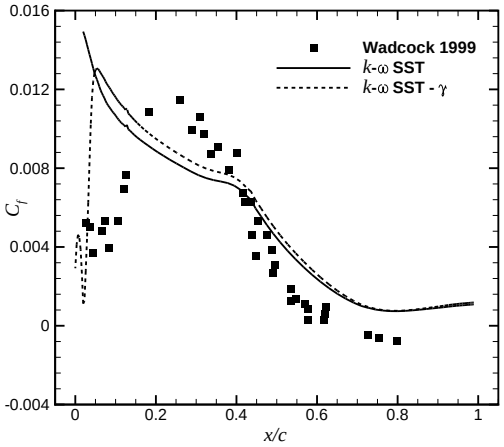

(b) $r/R = 0.28$.

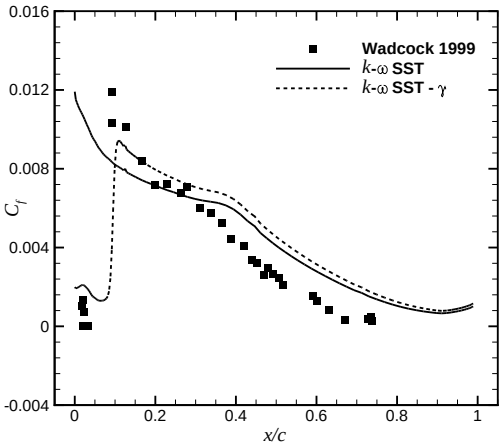

(c) $r/R = 0.50$.

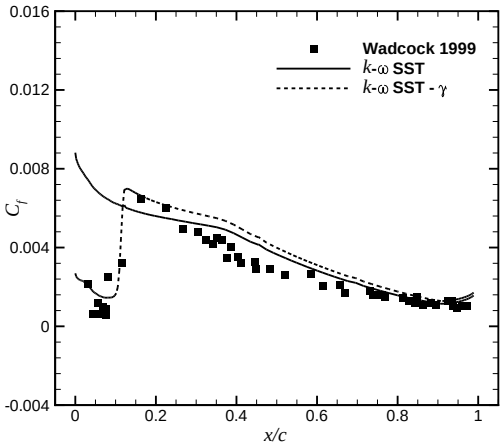

(d) $r/R = 0.72$.

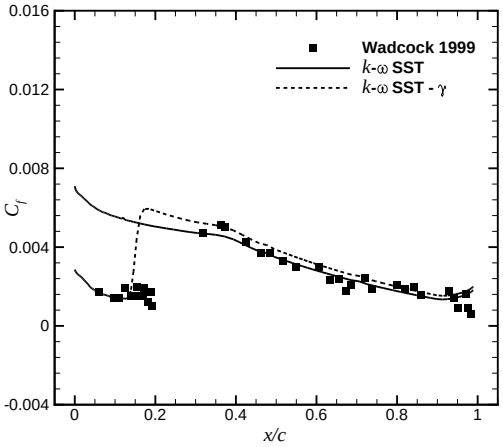

(e) $r/R = 0.83$.

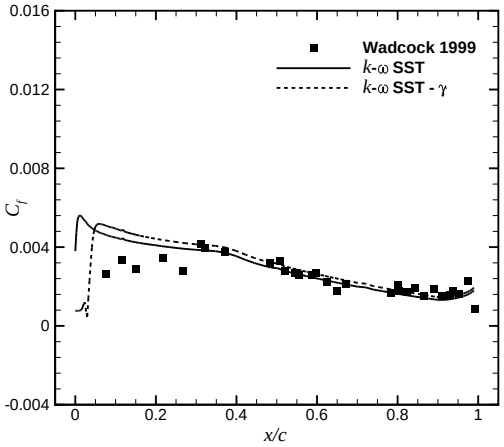

(f) $r/R = 0.94$.

Fig. 8: Comparison between the computed skin friction coefficient using a fully turbulent and transition model solutions with the experimental data of Wadcock *et al.*[37]. Conditions employed: $M_{\text{tip}} = 0.69$, $Re = 4.95 \cdot 10^6$, and $\theta_{75} = 10°$.

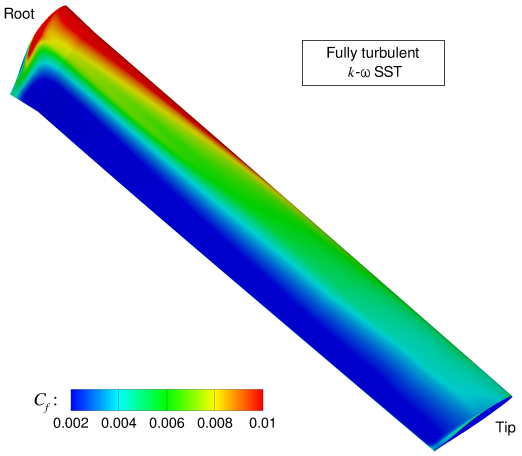

(a) Fully turbulent solution, $\theta_{75} = 3°$.

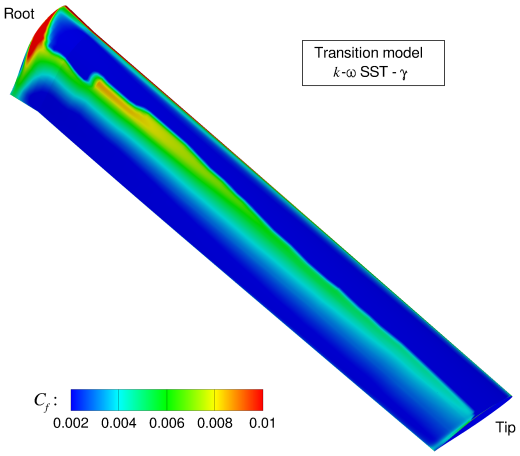

(b) Transition model solution, $\theta_{75} = 3°$.

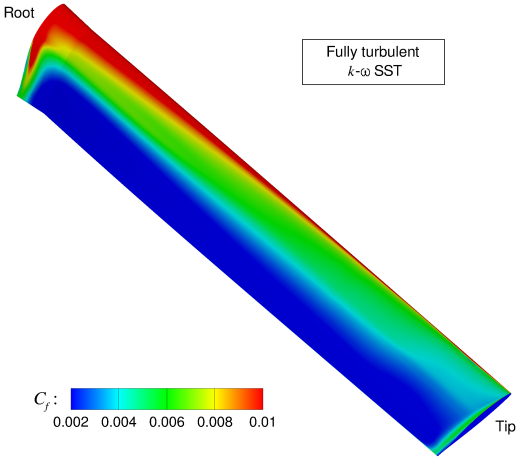

(c) Fully turbulent solution, $\theta_{75} = 10°$.

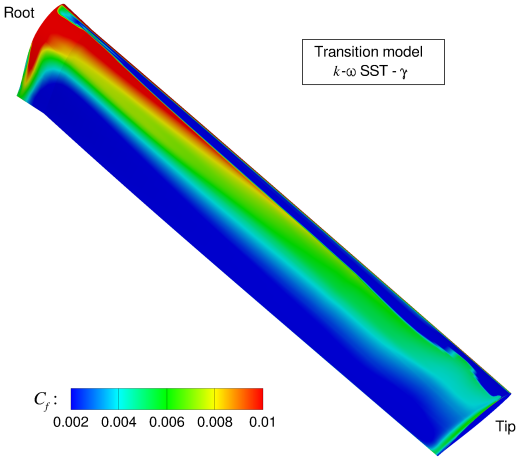

(d) Transition model solution, $\theta_{75} = 10°$.

Fig. 9: Surface skin friction coefficient for the fully turbulent and transition model cases.

B. Results for the PSP Rotor

A study of the performance of the PSP (Pressure Sensitive Paint) rotor in hover was also carried out. The blade-tip Mach number was set to 0.65, and seven collective pitch angles were considered, from θ_{75}=6^o to 12^o with a delta of 1 degree. The Reynolds number, based on the reference blade chord of 5.45 inches and on the tip speed, was $2.16 \cdot 10^6$. Figure 10 shows the figure of merit (left) and blade torque coefficient C_Q/σ (right) as functions of the blade loading coefficient C_T/σ for the PSP blade. Momentum-based estimates of the figure of merit are also included, where induced power factors k_i of 1.1 and 1.15, and overall profile drag coefficient C_D of 0.01 were used. No experimental data is available at present for further comparisons.

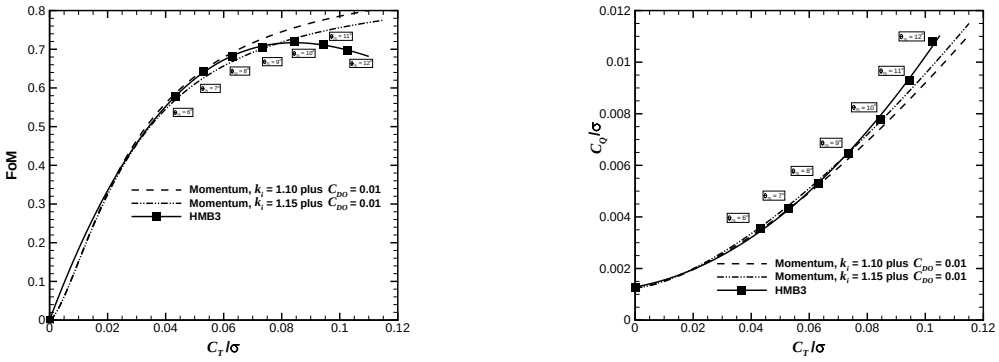

(a) FoM - C_T/σ.

(b) C_Q/σ - C_T/σ.

Fig. 10: Figure of merit (left) and blade torque coefficient (right) as function of the blade loading coefficient for the PSP rotor. Conditions employed: $M_{\text{tip}} = 0.65$, $Re = 2.16 \cdot 10^6$, and Menter's k-ω SST turbulence model[29].

An overview of the surface pressure coefficient at collective pitch angle of 11^o is shown in Figure 11a. The flowfield below the PSP blade is visualised by iso-surfaces of Q-criterion (Figure 11b). The computations captured the rotor wake up to 3-4 blade passages.

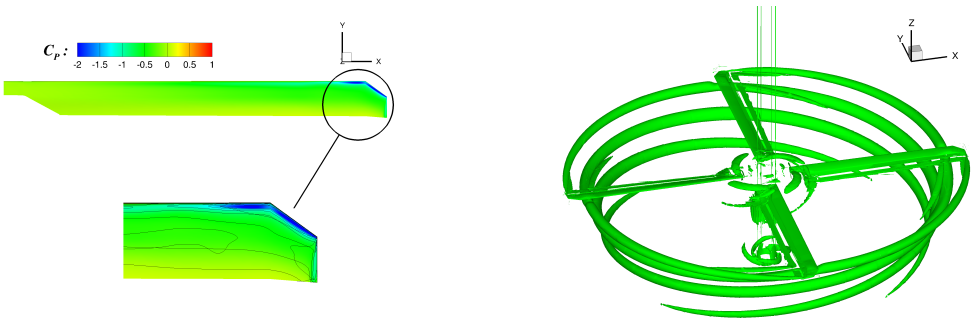

(a) (b)

Fig. 11: Surface pressure coefficient (left) and wake of the PSP rotor blade. Conditions employed: $M_{\text{tip}} = 0.65$, $Re = 2.16 \cdot 10^6$, θ_{75}=11^o, and Menter's k-ω SST turbulence model[29].

VI. Conclusions

Fully turbulent and transitional flow solutions were obtained for the XV-15 tiltrotor blade in hover. The results of CFD compare well with test data for the integrated blade load. The transport-based transition model captured well the evolution of the transition but this did not affect the integral aerodynamic loads. Nevertheless, adding the transition model did not result in more expensive computations and the solutions were obtained starting from a clean initial state, showing the robustness of the transport-based model. The work with the XV-15 is to be extended to include unsteady computations in addition to the steady-state results presented here. The employed chimera method resulted in mesh savings over previous studies even if the accuracy of the results was increased. Regarding the PSP blade results, experimental data is necessary for detailed comparisons. The agreement with the theory for the integrated loads is, however, encouraging.

Acknowledgements

The use of the cluster Chadwick of the University of Liverpool is gratefully acknowledged. Some results were obtained using the EPSRC funded ARCHIE-WeSt High Performance Computer (`www.archie-west.ac.uk`), EPSRC grant no. EP/K000586/1. Part of this work is funded under the HiperTilt Project of the UK Technology Strategy Board (TSB) and Leonardo Helicopters under Contract Nr. 101370.

[1] Maisel, M. D., Giulianetti, D. J., and Dugan, D. C., "The History of the XV-15 Tilt Rotor Research Aircraft: From Concept to Flight," NASA SP-2000-4517, Feb. 2000.

[2] Potsdam, M. A., Schaller, D. F., Rajagopalan, R. G., and Silva, M. J., "Tilt Rotor Aeromechanics Phenomena in Low Speed Flight," *Proceedings of the Fourth Decennial Specialist's Conference on Aeromechanics*, AHS, San Francisco, CA, 2004, pp. 1–13.

[3] Narducci, R., Jiang, F., Liu, J., and Clark, R., "CFD Modeling of Tiltrotor Shipboard Aerodynamics with Rotor Wake Interactions," *Proceedings of the Twenty Seventh Applied Aerodynamics Conference*, AIAA, San Antonio, Texas, 2009, pp. 1–13.

[4] "AugustaWestland AW609," http://www.agustawestland.com/product/aw609, last visited data: 22/11/2015.

[5] Harris, J. C., Scheidler, P. F., Hopkins, R., and Fortenbaugh, R. L., "Initial Power-off Testing of the BA609 Tiltrotor," *Proceedings of the Sixty-Sixth Annual Forum*, AHS, Phoenix, Arizona, 2000, pp. 1–9.

[6] "Advancement of Proprotor Technology, Task II - Wind-Tunnel Test Results," NASA CR–114363, Sept. 1971.

[7] Weiberg, J. A. and Maisel, M. D., "Wind-Tunnel Tests of the XV-15 Tilt Rotor Aircraft," NASA TM–81177, April 1980.

[8] Felker, F. F., Betzina, M. D., and Signor, D. B., "Performance and Loads Data from a Hover Test of a Full-Scale XV-15 Rotor," NASA TM–86833, Sept. 1985.

[9] Bartie, K., Alexander, H., McVeigh, M., Mon, S. L., and Bishop, H., "Hover Performance Tests of Baseline Meter and Advanced Technology Blade (ATB) Rotor Systems for the XV-15 Tilt Rotor Aircraft," NASA CR–114626, Oct. 1986.

[10] Light, J. S., "Results from an XV-15 Rotor Test in the National Full-Scale Aerodynamics Complex," *Proceedings of the 53rd American Helicopter Society Annual Forum*, AHS, Virginia Beach, Virginia, 1997.

[11] Betzina, M. D., "Rotor Performance of an Isolated Full-Scale XV-15 Tiltrotor in Helicopter Mode," *Proceedings of the American Helicopter Society Aerodynamics, Acoustics, and Test and Evaluation Technical Specialist Meeting*,

AHS, San Francisco, CA, 2002, pp. 1–12.

[12] Wadcock, A. J., Yamauchi, G. K., and Driver, D. M., "Skin Friction Measurements on a Hovering Full-Scale Tilt Rotor," *Journal American Helicopter Society*, Vol. 99, No. 4, 1999, pp. 312–319.

[13] Kaul, U. K. and Ahmad, J., "Skin Friction Predictions Over a Hovering Tilt-Rotor Blade Using OVERFLOW2," *Proceedings of the Twenty-Ninth Applied Aerodynamics Conference*, AIAA, Honolulu, Hawaii, 2011, pp. 1–19.

[14] Kaul, U. K., "Effect of Inflow Boundary Conditions on Hovering Tilt-Rotor Flows," *Proceedings of the Seventh International Conference on Computational Fluid Dynamics*, ICCFD7, Big Island, Hawaii, 2012, pp. 1–19.

[15] Spalart, P. R. and Allmaras, S., "A One-Equation Turbulence Model for Aerodynamic Flows," *La Recherche Aérospatiale*, , No. 1, 1994, pp. 5–21.

[16] Yoon, S., Pulliam, T. H., and Chaderjian, N. M., "Simulations of XV-15 Rotor Flows in Hover Using OVERFLOW," *Proceedings of the Fifth Decennial AHS Aeromechanics Specialists*, AHS, San Francisco, CA, 2014, pp. 1–11.

[17] Sheng, C. and Zhao, Q., "Investigations of XV-15 Rotor Hover Performance and Flow Field Using U2NCLE and HELIOS Codes," *Proceedings of the Fifty-Fourth Aerospace Sciences Meeting*, AIAA, San Diego, California, 2016, pp. 1–18.

[18] Gates, S., "Aerodynamic Analysis of Tiltrotors in Hovering and Propeller Modes Using Advanced Navier-Stokes Computations," *Proceedings of the Thirty-Ninth European Rotorcraft Forum*, ERF, Moscow, Russia, 2013, pp. 1–26.

[19] Abras, J. and Narducci, R., "Analysis of CFD Modeling Techniques over the MV-22 Tiltrotor," *Proceedings of the Sixty-Sixth Annual Forum*, AHS, Phoenix, AZ, 2010, pp. 1–11.

[20] Watkins, A. N., Leighty, B. D., Lipford, W. E., Goodman, K. Z., Crafton, J., and Gregory, J. W., "Measuring Surface Pressures on Rotor Blades Using Pressure-Sensitive Paint," *AIAA Journal*, Vol. 54, No. 1, 2016, pp. 206–215, DOI:http://dx.doi.org/10.2514/1.J054191.

[21] Lawson, S. J., Steijl, R., Woodgate, M., and Barakos, G. N., "High performance computing for challenging problems in computational fluid dynamics," *Progress in Aerospace Sciences*, Vol. 52, No. 1, 2012, pp. 19–29, DOI: 10.1016/j.paerosci.2012.03.004.

[22] Steijl, R. and Barakos, G. N., "Sliding mesh algorithm for CFD analysis of helicopter rotor-fuselage aerodynamics," *International Journal for Numerical Methods in Fluids*, Vol. 58, No. 5, 2008, pp. 527–549, DOI: 10.1002/d.1757.

[23] Steijl, R., Barakos, G. N., and Badcock, K., "A framework for CFD analysis of helicopter rotors in hover and forward flight," *International Journal for Numerical Methods in Fluids*, Vol. 51, No. 8, 2006, pp. 819–847, DOI: 10.1002/d.1086.

[24] Osher, S. and Chakravarthy, S., "Upwind schemes and boundary conditions with applications to Euler equations in general geometries," *Journal of Computational Physics*, Vol. 50, No. 3, 1983, pp. 447–481, DOI: 10.1016/0021-9991(83)90106-7.

[25] Roe, P. L., "Approximate Riemann Solvers, Parameter Vectors, and Difference Schemes," *Journal of Computational Physics*, Vol. 43, No. 2, 1981, pp. 357–372, DOI: 10.1016/0021-9991(81)90128-5.

[26] van Leer, B., "Towards the ultimate conservative difference scheme. V.A second-order sequel to Godunov's Method," *Journal of Computational Physics*, Vol. 32, No. 1, 1979, pp. 101–136, DOI: 10.1016/0021-9991(79)90145-1.

[27] van Albada, G. D., van Leer, B., and Roberts, W. W., "A Comparative Study of Computational Methods in Cosmic Gas Dynamics," *Astronomy and Astrophysics*, Vol. 108, No. 1, 1982, pp. 76–84.

[28] Axelsson, O., *Iterative Solution Methods*, Cambridge University Press: Cambridge, MA, 1994.

[29] Menter, F. R., "Two-Equation Eddy-Viscosity Turbulence Models for Engineering Applications," *AIAA Journal*, Vol. 32, No. 8, 1994, pp. 1598–1605, DOI: 10.2514/3.12149.

[30] Menter, F. R., Smirnov, P. E., Liu, T., and Avancha, R., "A One-Equation Local Correlation-Based Transition Model," *Flow Turbulence Combust*, Vol. 95, No. 4, 2015, pp. 583–619, DOI:10.1007/s10494-015-9622-4.

[31] Menter, F., Langrtry, R., Rikki, R., Suzen, S., Huang, P., and Volker, S., "A Correlation-Based Transition Model Using Local Variables - Part I: Model Formulation." *Journal of Turbomachinery*, Vol. 128, No. 3, 2006, pp. 1598–1605.

[32] Acree, C., "Rotor Design Options for Improving XV-15 Whirl-Flutter Stability Margins," NASA TP–2004-212262, March 2004.

[33] Noonan, K. W., "Aerodynamic Characteristics of Two Rotorcraft Airfoils Designed for Application to the Inboard Region of a Main Rotor Blade," NASA TP-3009, U.S. Army Aviation Systems Command, TR-90-B-005, July 1990.

[34] Noonan, K. W., "Aerodynamic Characteristics of Two Rotorcraft Airfoils Designed for Application to the Inboard Region of a Main Rotor Blade," NASA TM-4264, U.S. Army Aviation Systems Command, TR-91-B-003, May 1991.

[35] Brocklehurst, A., *High Resolution Method for the Aerodynamic Design of Helicopter Rotors*, Ph.D. thesis, University of Liverpool, UK, June 2013.

[36] Spalart, P. R. and Allmaras, S. R., "A One-Equation Turbulence Model for Aerodynamic Flows," *La Recherche Aérospatiale*, 1994, pp. 5–21.

[37] Wadcock, A. J., Yamauchi, G. K., and Driver, D. M., "Skin Friction Measurements on a Hovering Full-Scale Tilt Rotor," *Journal of the American Helicopter Society*, Vol. 44, No. 4, 1999, pp. 321–319, DOI: http://dx.doi.org/10.4050/JAHS.44.312.